Opto-Electronic Advances

Supplementary information

September 2024, Vol. 7, No. 9

DOI: 10.29026/oea.2024.240045

Complete-basis-reprogrammable coding metasurface for generating dynamically-controlled holograms under arbitrary polarization states

Zuntian Chu[1,2†], Xinqi Cai[1,2†], Ruichao Zhu[1,2*], Tonghao Liu[3*], Huiting Sun[1,2], Tiefu Li[1,2], Yuxiang Jia[1,2], Yajuan Han[1,2], Shaobo Qu[1,2] and Jiafu Wang[1,2*]

[1]Shaanxi Key Laboratory of Artificially-Structured Functional Materials and Devices, Air Force Engineering University, Xi'an 710051, China; [2]Suzhou Laboratory, Suzhou 215000, China; [3]Zhijian Laboratory, Rocket Force University of Engineering, Xi'an 710025, China.

[†]These authors contributed equally to this work.

*Correspondence: RC Zhu, E-mail: zhuruichao1996@163.com; TH Liu, E-mail: liutonghaor@163.com;
JF Wang, E-mail: wangjiafu1981@126.com

This file includes:

Section 1: Discussion of dynamic AA Phase modulation mechanism
Section 2: Determination of the optimal PIN diodes' locations
Section 3: Schematic demonstration in terahertz spectra
Section 4: Jones matrix analysis and designed details of the proposed meta-particle
Section 5: Overall Schematics of the CBR-CM Prototype
Section 6: Structural configuration and simulated co-polarized reflection performance of the super-cell
Section 7: Flow chart of the iterative optimization algorithm
Section 8: Simulated and measured broadband performance of meta-holograms with identical focal length
Section 9: Simulated and measured broadband performance of meta-holograms with variable focal length
Section 10: Simulated and measured broadband performance of meta-holograms with switchable spatial pixels
Section 11: Theoretical prediction of three groups of different meta-holograms and analysis and discussion
Section 12: Holographic imaging manipulation principle under orthogonal LP conversion channels
Section 13: Simulated and measured broadband performance of meta-holograms against arbitrary polarization states on Poincaré sphere
Section 14: Performance comparison of the proposed CBR-CM with previous works of reprogrammable metasurfaces
Section 15: Diagram of the FPGA-based control circuit
Section 16: The photographs of fabricated metasurface and experimental setup

Supplementary information for this paper is available at https://doi.org/10.29026/oea.2024.240045

Section 1: Discussion of dynamic AA phase modulation mechanism

According to the optical Coriolis effect, the rotational Doppler shift occurs when a light beam carrying angular momentum propagates through a spinning object along its rotation axis, and the corresponding angular frequency $\Delta\omega$ will lead to the generation of geometric phase $\Delta\varphi_{\rm g}$, which can be expressed as

$$\Delta\varphi_{\rm g} = \int \Delta\omega {\rm d}t = \int \sigma\Omega_z {\rm d}t\,, \tag{S1}$$

where Ω_z is the angular velocity of the spinning object, and σ=±1 respectively represent the spin directions of two orthogonal CP waves. Actually, the rotation of the object can be regarded as a conversion of the polarization state, corresponding to the rotation of the polarization ellipse on Poincaré sphere. Since each latitude line on Poincaré sphere represents an evolutionary state of CP conversion containing geometric phase. Thereupon, the angular velocity of the spinning object can be equivalent to the rotation velocity of the polarization ellipse; i.e. Ω_z=d(2$\tau\theta$)/dt, in which θ and τ=±1 separately depict the rotation angle and rotation direction of the polarization ellipse. Then, Eq. (S1) is simplified as

$$\varphi_{\rm g} = 2\int \sigma\tau {\rm d}\theta = 2\int \delta {\rm d}\theta\,, \tag{S2}$$

where δ=+1 represents the opposite spin direction of the incident wave and rotation direction of the polarization ellipse; δ=−1 represents the identical spin direction of the incident wave and rotation direction of the polarization ellipse. On the one hand, the surface currents on the umbrella-shaped structure are mainly concentrated in the motion of the two-arm arc structures. On the other hand, the changes of the two-arm arc structures depend on the evolution of their respective corresponding central angles. Thus, the phase shift provided by the umbrella-shaped structure is determined by the starting position and ending position of the path evolution. According to the geometric configuration of the meta-particle structure and the surface currents distributions path corresponding to the "ON" and "OFF" states of the PIN diodes under orthogonal CP incidence shown in Fig. 2(d) and 2(e), the start position of the evolution path for different diode states is different, and the ending position is at the end of two-arm arc structures, where the incidence of LCP wave corresponds to the surface currents path of the left arm, and the incidence of RCP wave corresponds to the surface currents path of the right arm. Combined with Eq. (S2), the AA geometric phase obtained via path effect under orthogonal CP incidence can be calculated as

$$\begin{cases} \Phi_{\rm LL}^{\rm AA} = 2\int_{\theta_{\rm sL}}^{\theta_{\rm eL}} {\rm d}\theta_{\rm L} \\ \Phi_{\rm RR}^{\rm AA} = 2\int_{\theta_{\rm sR}}^{\theta_{\rm eR}} {\rm d}\theta_{\rm R} \end{cases}, \tag{S3}$$

where $\Phi_{\rm LL}^{\rm AA}$ and $\Phi_{\rm RR}^{\rm AA}$ are the co-polarized reflection AA phase imparted by the meta-particle to, respectively, the LCP and RCP waves. $\theta_{\rm sL}$ and $\theta_{\rm eL}$, $\theta_{\rm sR}$ and $\theta_{\rm eR}$ are respectively defined as the starting position and ending position of the path evolution to corresponding polarization waves. As analyzed above, considering the handedness of incident orthogonal CP waves, for the "ON" and "OFF" states of the PIN diodes, the co-polarized reflection phase difference between "1" and "0" can be deduced as

$$\begin{cases} \Delta\Phi_{\rm LL}^{\rm AA} = 2\int_{\theta_{\rm sL2}}^{\theta_{\rm eL2}} {\rm d}\theta_{\rm L} - 2\int_{\theta_{\rm sL1}}^{\theta_{\rm eL1}} {\rm d}\theta_{\rm L} = 2(\theta_{\rm sL1} - \theta_{\rm sL2}) \\ \Delta\Phi_{\rm RR}^{\rm AA} = 2\int_{-\theta_{\rm sR2}}^{-\theta_{\rm eR2}} {\rm d}\theta_{\rm R} - 2\int_{-\theta_{\rm sR1}}^{-\theta_{\rm eR1}} {\rm d}\theta_{\rm R} = 2(\theta_{\rm sR2} - \theta_{\rm sR1}) \end{cases}, \tag{S4}$$

herein, $\theta_{\rm eL1}$ is equal to $\theta_{\rm eL2}$, and $\theta_{\rm eR1}$ is equal to $\theta_{\rm eR2}$. Therefore, one can obtain the co-polarized reflection AA phase difference via the difference of the starting positions of surface currents distribution paths under different states of PIN diodes.

Section 2: Determination of the optimal PIN diodes' locations

As illustrated in Fig. 2(a), the two PIN diodes of the meta-particles are symmetrically stabilized in the approximately middle part of the umbrella-shaped structure. To intuitively and accurately analyze and determine the impact resulting from positional variation of the PIN diodes, herein, we take the incidence of LCP wave as an example to simulate the co-polarized reflection amplitude response via only altering the α values of the two arms. As illustrated in Fig. S1, the overall co-polarized reflection amplitude is remained at about 0.9 over 9–10.5 GHz when fixing the two PIN diodes to

the slotted position at about the central line of the maximum central angle of two arms. In fact, as the central angles corresponding to the PIN diodes of the two arms decrease, the "ON-OFF" effect of the PIN diodes for individual modulation is weakened and the mutual coupling is enhanced, leading to the reduced co-polarized reflection efficiency. In consideration of the actual package dimensions of the PIN diodes and in order to obtain higher co-polarized reflection amplitudes and lower the coupling, the values of α are meticulously optimized and eventually determined as 70°.

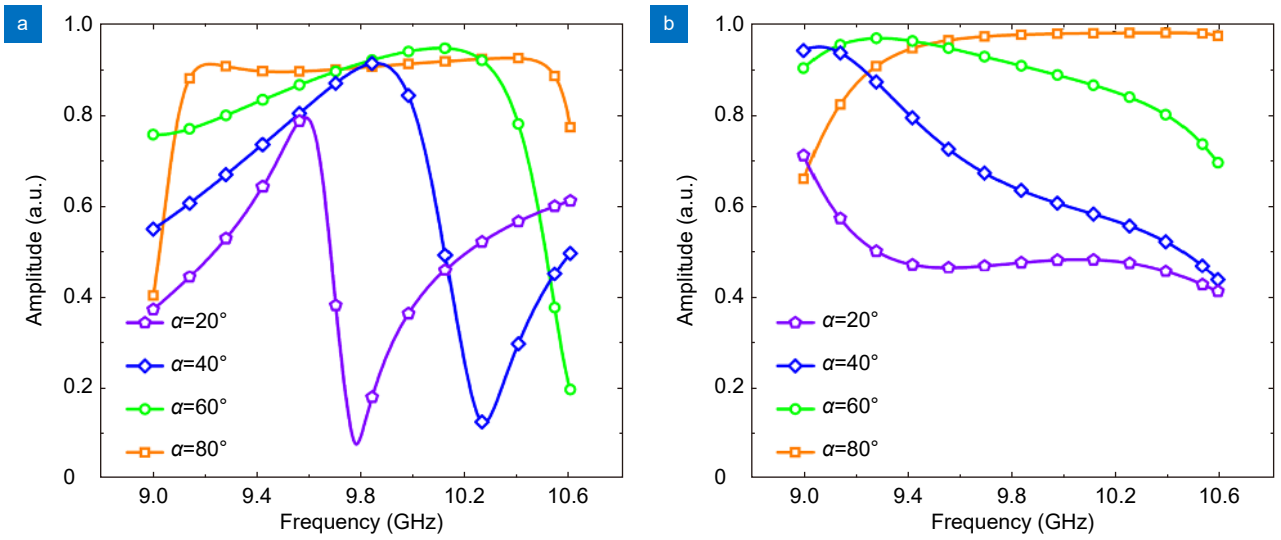

Fig. S1 | Reflection amplitude responses of the proposed meta-particle under LCP normal incidence. (**a**) Simulated co-polarized reflection amplitudes with coding states of "11" and "10" varying against different central angles α. (**b**) Simulated co-polarized reflection amplitudes with coding states of "01" and "00" varying against different central angles α.

Section 3: Schematic demonstration in terahertz spectra

Herein, in the design of the dynamic achiral meta-particle in terahertz spectra, we selected VO_2 as an alternative substance and embedded it into the identical structure illustrated in Fig. 2(a), constructed the model and performed numerical simulations. The topological configuration of the meta-particle is shown in Fig. S2(a), where the basic element is composed of two layers of noble metal film separated by one layer of pure dielectric spacer. Specifically, the metallic backplate (Au, electric conductivity σ=4.56×10^7 S/m) at the bottom layer and the dielectric cavity (polyimide, loss tangent tanδ=0.0027, dielectric constant ε_r=3.5) at the middle layer are respectively utilized to reflect the incident waves and increase the propagation phase shift. Also, due to the reversible insulator-metal-transition (IMT) of VO_2, both arms of the umbrella structure (Au, electric conductivity σ=4.56×10^7 S/m) at the top layer can be flexibly and dynamically switched between cutoff condition when the VO_2 is in the insulating state (electric conductivity σ=1×10^3 S/m) and conduction condition when the VO_2 is in the metallic state (electric conductivity σ=5×10^5 S/m). And other parameters in the meta-particle are schematically shown in Fig. S2(a). Correspondingly, each coding meta-particle has four states: "ON/ON", "ON/OFF", "OFF/ON", and "OFF/OFF". For the sake of simplification, four states are respectively defined as "11", "10", "01", and "00" and the former and the latter of the two-bit codes represent the co-polarized reflection phases under the illumination of LCP and RCP wave. We next investigate and analyze the reflection EM responses of the designed meta-particle with commercial simulation software and the simulated amplitude and phase profiles of reflection spectra are plotted in Fig. S2(b–e) for different coding states under the normal incidence of orthogonal CP waves. Within a relatively broad frequency band 0.8–1.1 THz, it's clearly noted that the phases difference of LCP or RCP co-polarized reflected waves when the VO_2 changes from insulating state to metallic state can be approximately maintained 180° with an average of 0.9 reflection amplitudes, which are in good agreement with the theoretical predications. In addition, we remark that, when the LCP or RCP wave propagates normally into the meta-particle, altering the working state of the VO_2 in the cross-polarization direction has no effect on the co-polarized reflection amplitude and phase

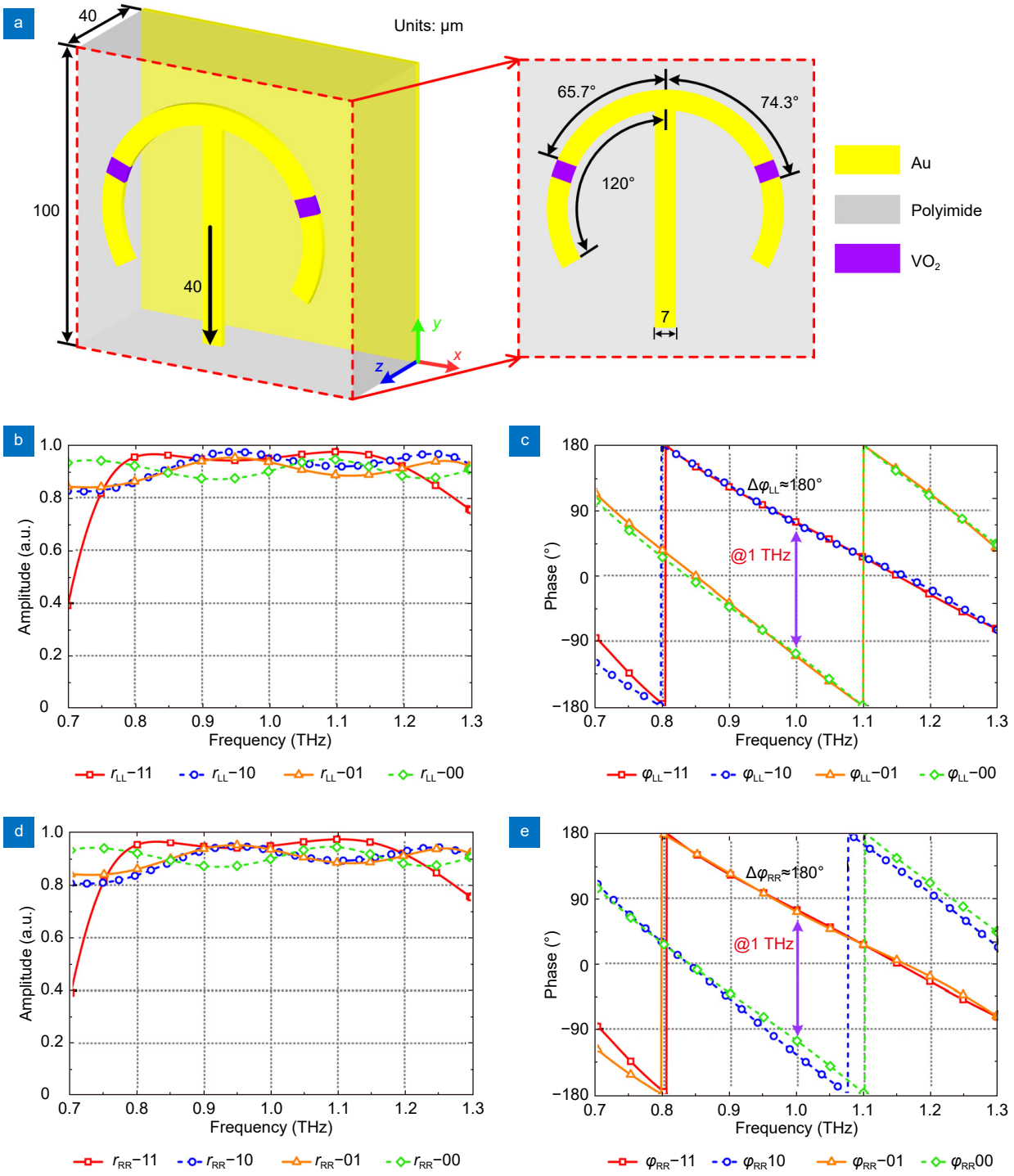

Fig. S2 | Design and EM responses of the dynamic achiral meta-particle in terahertz spectra. (**a**) Topological layout of an elementary meta-particle and corresponding umbrella-shaped structure in the top layer. The geometric parameters are denoted in the figure. (a, **b**) Simulated co-polarized reflection amplitude and phase responses of the proposed meta-particle with coding states of "11", "10", "01", and "00" under LCP normal incidence, respectively. (**c**, **d**) Simulated co-polarized reflection amplitude and phase responses of the proposed meta-particle with coding states of "11", "10", "01", and "00" under RCP normal incidence, respectively.

responses, which indicates that the realized meta-particle has high polarization stability and cross-polarization isolation. Therefore, when constructing the reconfigurable meta-holograms, the well-defined images can be reproduced and hidden via arranging the meta-particles with and without embedded VO_2 according to the pre-designed phase patterns. Furthermore, combined with the individually addressable techniques in two-dimensional plane, high-precision control

of phase responses of each meta-particle on the metasurface can be achieved, allowing reconstruction and transformation of any holographic image. It should be noted that the meta-particle only achieves predesigned dynamic phase response through embedded VO_2 with thermally controlled reconfigurability. However, through incorporating other well-established switchable and alternative configurations such as Schottky diodes and liquid crystals driven by externally electrical stimuli and optical phase-change materials like GeTe and Sb_2S_3 into the optimized meta-particle design, it's possible to fabricate the CBR-CM for generating dynamically-controlled holograms under arbitrary polarization states in terahertz or infrared or visible frequencies, and the working principle is essentially the same.

Section 4: Jones matrix analysis and designed details of the proposed meta-particle

The complex Jones matrix describes the incidence and reflection of EM wave passing through the meta-particle. When two orthogonal CP waves are vertically incident, taking into accounting the opposite propagation direction between the incident and reflected waves, the complex amplitude profiles of the reflected electric field can be represented via the incident electric field and complex Jones matrix $\boldsymbol{R}_{\rm cir}$ representing CP basis as

$$\begin{pmatrix} E_{\rm R}^{r} \\ E_{\rm L}^{r} \end{pmatrix} = \boldsymbol{R}_{\rm cir} \begin{pmatrix} E_{\rm L}^{i} \\ E_{\rm R}^{i} \end{pmatrix} = \begin{pmatrix} R_{\rm RL} & R_{\rm RR} \\ R_{\rm LL} & R_{\rm LR} \end{pmatrix} \begin{pmatrix} E_{\rm L}^{i} \\ E_{\rm R}^{i} \end{pmatrix} , \tag{S5}$$

where, $E_{\rm L/R}^{\rm i}$ ($E_{\rm L/R}^{\rm r}$) denote input (output) electric field of LCP and RCP wave and $R_{\rm LL} = r_{\rm LL} \cdot {\rm e}^{{\rm i}\varphi_{\rm LL}}$ ($R_{\rm RR} = r_{\rm RR} \cdot {\rm e}^{{\rm i}\varphi_{\rm RR}}$) and $R_{\rm RL} = r_{\rm RL} \cdot {\rm e}^{{\rm i}\varphi_{\rm RL}}$ ($R_{\rm LR} = r_{\rm LR} \cdot {\rm e}^{{\rm i}\varphi_{\rm LR}}$) are co- and cross-polarized complex reflection coefficients of LCP (RCP) wave, respectively. Assume that the Cartesian coordinate system is taken as the reference coordinate system under LP basis, then relationship between the incident and reflected electric field under LP wave incidence can be related via complex Jones matrix $\boldsymbol{R}_{\rm lin}$

$$\begin{pmatrix} E_{X}^{\rm r} \\ E_{Y}^{\rm r} \end{pmatrix} = \boldsymbol{R}_{\rm lin} \begin{pmatrix} E_{\rm X}^{i} \\ E_{\rm Y}^{\rm i} \end{pmatrix} = \begin{pmatrix} R_{\rm xx} & R_{\rm xy} \\ R_{\rm yx} & R_{\rm yy} \end{pmatrix} \begin{pmatrix} E_{\rm X}^{i} \\ E_{\rm Y}^{\rm i} \end{pmatrix} , \tag{S6}$$

where, $E_{X/Y}^{\rm i}$ ($E_{X/Y}^{\rm r}$) depict input (output) electric field polarized along x-/y-direction and $R_{xx} = r_{xx} \cdot {\rm e}^{{\rm i}\varphi_{xx}}$ ($R_{yy} = r_{yy} \cdot {\rm e}^{{\rm i}\varphi_{yy}}$) and $R_{yx} = r_{yx} \cdot {\rm e}^{{\rm i}\varphi_{yx}}$ ($R_{xy} = r_{xy} \cdot {\rm e}^{{\rm i}\varphi_{xy}}$) are co- and cross-polarized complex reflection coefficients of x- (y-) LP wave, separately.

Since the CP basis vectors and LP basis vectors illustrated in Eqs. (S5) and (S6) meet the relationship

$$\begin{pmatrix} E_{\rm L}^{i} \\ E_{\rm R}^{i} \end{pmatrix} = \begin{pmatrix} 1 & -{\rm i} \\ 1 & {\rm i} \end{pmatrix} \cdot \begin{pmatrix} E_{X}^{\rm i} \\ E_{Y}^{\rm i} \end{pmatrix} / \sqrt{2} \,\&\, \begin{pmatrix} E_{\rm R}^{r} \\ E_{\rm L}^{r} \end{pmatrix} = \begin{pmatrix} 1 & -{\rm i} \\ 1 & {\rm i} \end{pmatrix} \cdot \begin{pmatrix} E_{X}^{\rm r} \\ E_{Y}^{\rm r} \end{pmatrix} / \sqrt{2} \tag{S7}$$

By associating the above Equations, the relevance between $\boldsymbol{R}_{\rm cir}$ and $\boldsymbol{R}_{\rm lin}$ can be deduced as follows

$$\boldsymbol{R}_{\rm cir} = \boldsymbol{\Lambda} \cdot \boldsymbol{R}_{\rm lin} \cdot \boldsymbol{\Lambda}^{-1} , \tag{S8}$$

where $''\boldsymbol{\Lambda} = \begin{pmatrix} 1 & -{\rm i} \\ 1 & {\rm i} \end{pmatrix} / \sqrt{2}$ describes the orthogonal decomposition of CP basis vectors in the form of LP basis vectors. Therefore, one can further mathematically transform (Eq. S8) into

$$\boldsymbol{R}_{\rm cir} = \begin{pmatrix} R_{\rm RL} & R_{\rm RR} \\ R_{\rm LL} & R_{\rm LR} \end{pmatrix} = \begin{pmatrix} R_{xx} + R_{yy} + {\rm i}R_{xy} - {\rm i}R_{yx} & R_{xx} - R_{yy} - {\rm i}R_{xy} - {\rm i}R_{yx} \\ R_{xx} - R_{yy} + {\rm i}R_{xy} + {\rm i}R_{yx} & R_{xx} + R_{yy} - {\rm i}R_{xy} + {\rm i}R_{yx} \end{pmatrix} / 2 . \tag{S9}$$

Therefore, four specified co- and cross-polarized reflection states under orthogonal CP incidence separately maintaining one-to-one correspondence with operation states of the two PIN diodes can be denoted in CP basis as follows

$$\boldsymbol{R}_{\rm cir11} = \begin{pmatrix} 0 & 1 \\ 1 & 0 \end{pmatrix} / \boldsymbol{R}_{\rm cir10} = \begin{pmatrix} 0 & 1 \\ -1 & 0 \end{pmatrix} / \boldsymbol{R}_{\rm cir01} = \begin{pmatrix} 0 & -1 \\ 1 & 0 \end{pmatrix} / \boldsymbol{R}_{\rm cir00} = \begin{pmatrix} 0 & -1 \\ -1 & 0 \end{pmatrix} . \tag{S10}$$

Through comparing Equations (S9) and (S10), the required matrices in LP basis can be calculated as

$$\boldsymbol{R}_{\rm lin11} = \begin{pmatrix} 1 & 0 \\ 0 & -1 \end{pmatrix} / \boldsymbol{R}_{\rm lin10} = \begin{pmatrix} 0 & {\rm i} \\ {\rm i} & 0 \end{pmatrix} / \boldsymbol{R}_{\rm lin01} = \begin{pmatrix} 0 & -{\rm i} \\ -{\rm i} & 0 \end{pmatrix} / \boldsymbol{R}_{\rm lin00} = \begin{pmatrix} -1 & 0 \\ 0 & 1 \end{pmatrix} . \tag{S11}$$

To further prove such scattering properties for LP waves of the designed meta-particle, the co- and cross-polarized reflection coefficients are simulated with FDTD method in CST Microwave Studio, where unit cell boundary conditions are employed along x- and y-direction and the excitation is set as x- or y-polarized waves propagating along $-z$

direction. The simulated results of co-polarized and cross-polarized reflection coefficients for with different coding states under LP normal incidence are shown in Fig. S3. Clearly, Fig. S3(a) shows, for state "11", in the frequency band of 9–10.5 GHz, equal amplitude $|r_{xx}|\approx|r_{yy}|\approx1$ and 180° phase difference that $\varphi_{yy}-\varphi_{xx}\approx180°$ are observed at co-polarized reflection coefficients, while for the cross-polarized mode, the coefficients are of equal amplitudes and phase where $|r_{yx}|\approx|r_{xy}|\approx0$ and $\varphi_{yx}-\varphi_{xy}\approx0°$. Additionally, for state "10" or "01", equal amplitude $|r_{xx}|\approx|r_{yy}|\approx0$ and 0° phase difference that $\varphi_{yy}-\varphi_{xx}\approx0°$ are observed at co-polarized reflection coefficients, while for the cross-polarized mode, the coefficients are of equal amplitude $|r_{yx}|\approx|r_{xy}|\approx1$ and with phase difference that $\varphi_{yx}-\varphi_{xy}\approx0°$, as showcased in Fig. S3(b) and S3(c). The phase difference 180° between coding state "10" and "01" of φ_{yx} and φ_{xy} with the average amplitude $|r_{yx}|$ and $|r_{xy}|$ at 1 is also achieved from 9 to 10.5 GHz, which can be utilized to tailor the wavefronts under orthogonal LP conversion channels. On the hand, it's observed from Fig. S3(d) that for state "00", the amplitude and phase for co-polarized mode, the equal amplitude of $|r_{xx}|\approx|r_{yy}|\approx1$ and the phase difference $\varphi_{xx}-\varphi_{yy}\approx180°$ are achieved, while for the cross-polarized mode, the coefficients are of equal amplitudes and phases where $|r_{yx}|\approx|r_{xy}|\approx0$ and $\varphi_{yx}-\varphi_{xy}\approx0°$. Therefrom, the phase difference

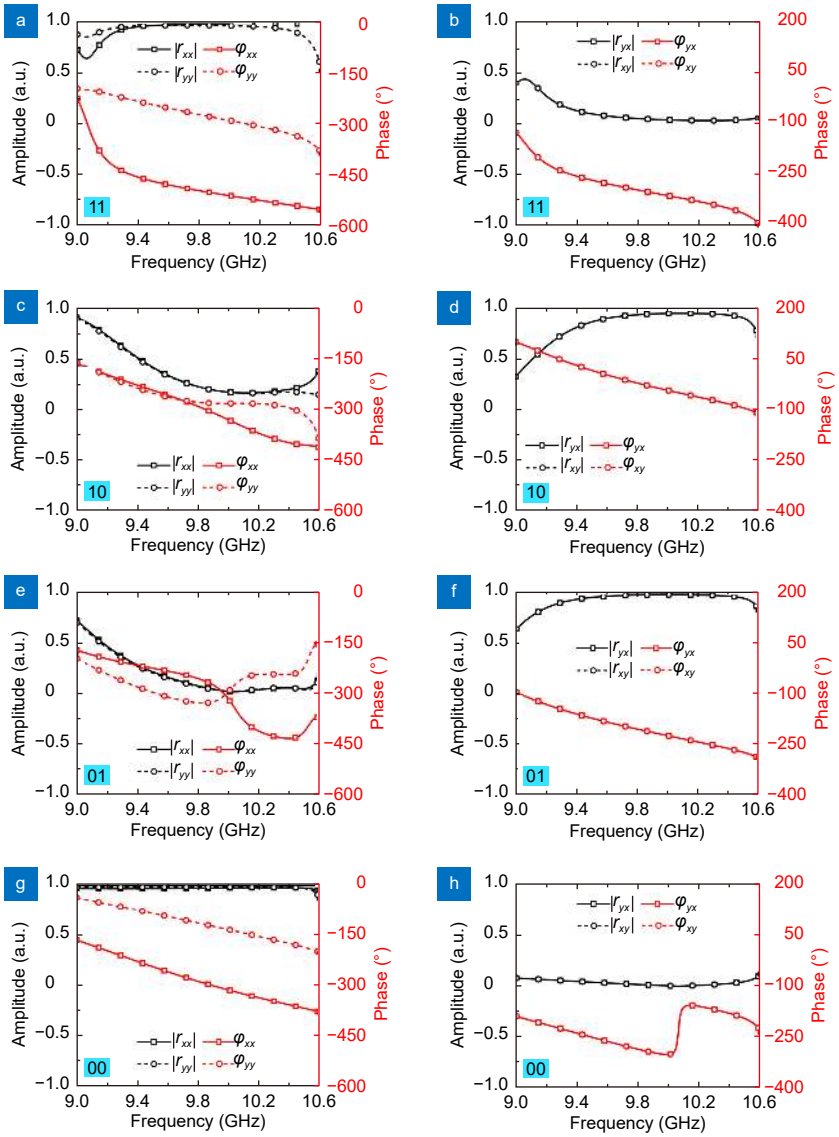

Fig. S3 | Reflection amplitude and phase responses of the proposed meta-particle with different coding states under orthogonal LP normal incidence. (**a**, **b**) Simulated co-polarized and cross-polarized reflection amplitudes and phases with coding states of "11". (**c**, **d**) Simulated co-polarized and cross-polarized reflection amplitudes and phases with coding states of "10". (**e**, **f**) Simulated co-polarized and cross-polarized reflection amplitudes and phases with coding states of "01". (**g**, **h**) Simulated co-polarized and cross-polarized reflection amplitudes and phases with coding states of "00".

180° between coding state "11" and "00" of φ_{xx} and φ_{yy} with the average amplitude $|r_{xx}|$ and $|r_{yy}|$ at 0.9 is also achieved from 9 to 10.5 GHz, which can be utilized to tailor the wavefronts under orthogonal LP preservation channels. Hence, it concludes that the designed meta-particles with desired complex Jones matrices $\boldsymbol{R}_{\text{lin}}$ are approximately realized in 9–10.5 GHz.

Section 5: Overall schematics of the CBR-CM prototype

The schematics of the top patch array, the middle ground, the DC bias network for for controlling co-polarized waves under RCP and LCP incidence are respectively denoted in Fig. S4. Coppers in different layers are marked by different colors (yellow, cyan, green, and blue). The substrates are represented in black.

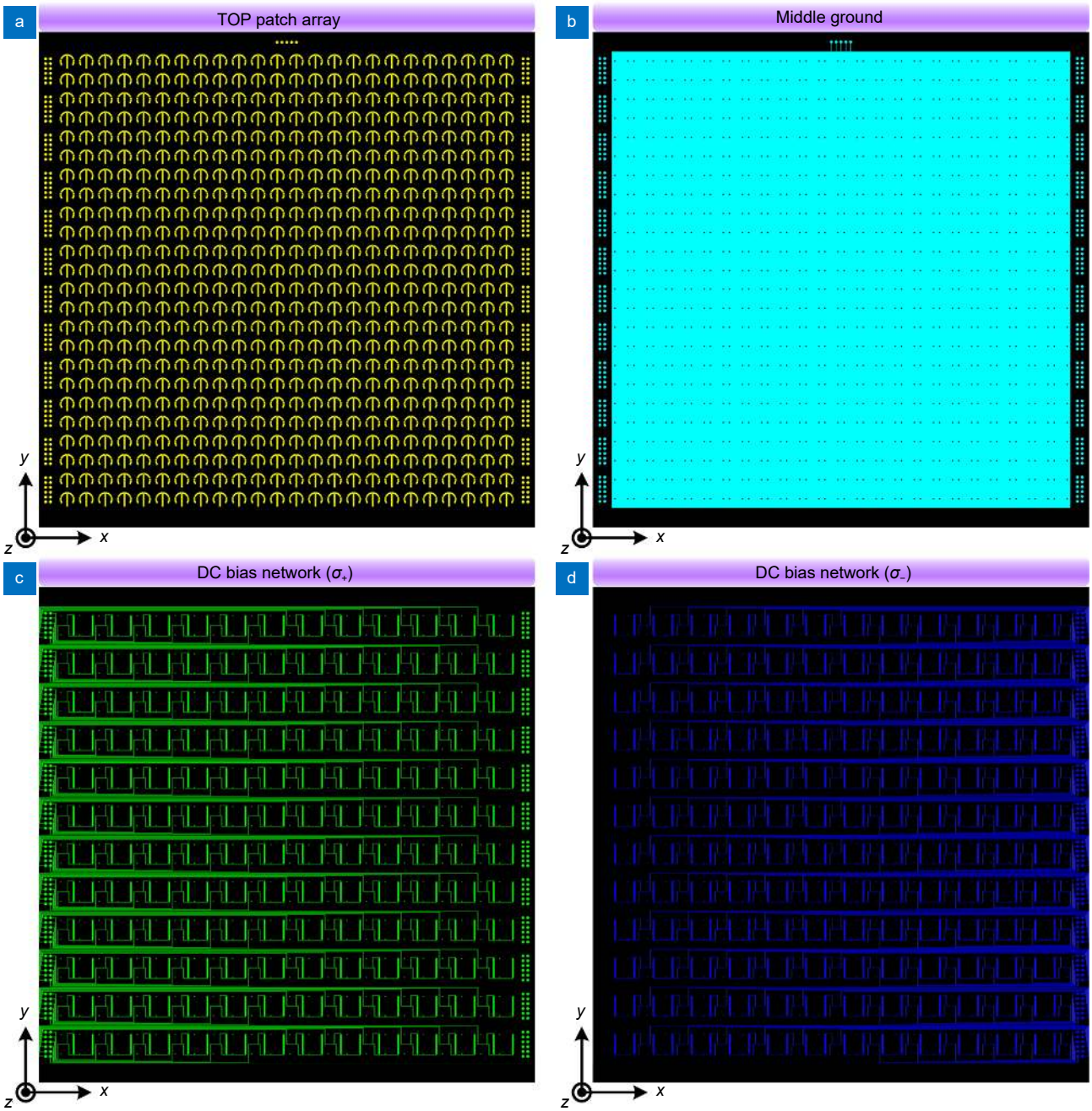

Fig. S4 | Schematic illustrations of the CBR-CM prototype. (**a**) The top patch array. (**b**) The middle ground. (**c**) The DC bias circuit controlling the coding meta-particles in R_r-R_i channel. (**d**) The DC bias circuit controlling the coding meta-particles in L_r-L_i channel.

Section 6: Structural configuration and simulated co-polarized reflection performance of the super-cell

Figure S5 displays the detailed structural layout of the coding super-cell, which consists of 2×2 coding meta-particles. To improve the resource utilization and simultaneously and independently supply the voltage for the PIN diodes in the left and right arms, only two meta-particles distributed along *y*-direction are connected via wide metallic lines and then separately join with the external DC bias lines to reduce the array coupling.

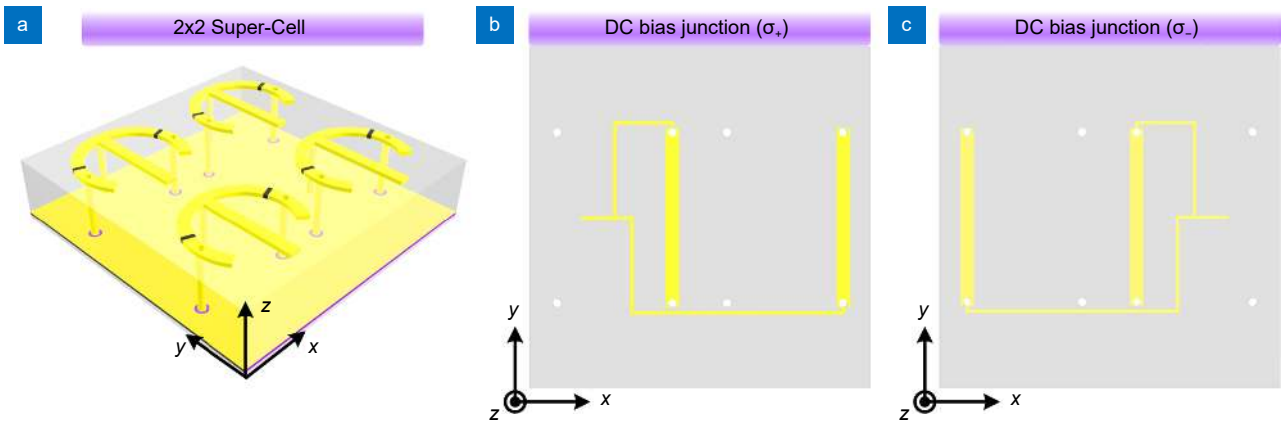

Fig. S5 | Structural layout of the 2×2 coding super-cell. (**a**) Perspective view of the proposed 2×2 super-cell. (**b**) The DC bias junction controlling the 2×2 coding super-cell in R_r-R_i channel. (**c**) The DC bias junction controlling the 2×2 coding super-cell in L_r-L_i channel.

The simulated co-polarized reflection amplitude and phase responses of the 2×2 coding super-cell are illustrated in Fig. S6. When the left or right four PIN diodes operate in "ON" or "OFF" state, the super-cell can provide 1-bit phase modulation for LCP or RCP incident waves. In addition, the simulated co-polarized reflection amplitude is observed to maintain on average above 0.9 for all coding states, demonstrating good amplitude-phase modulation performance.

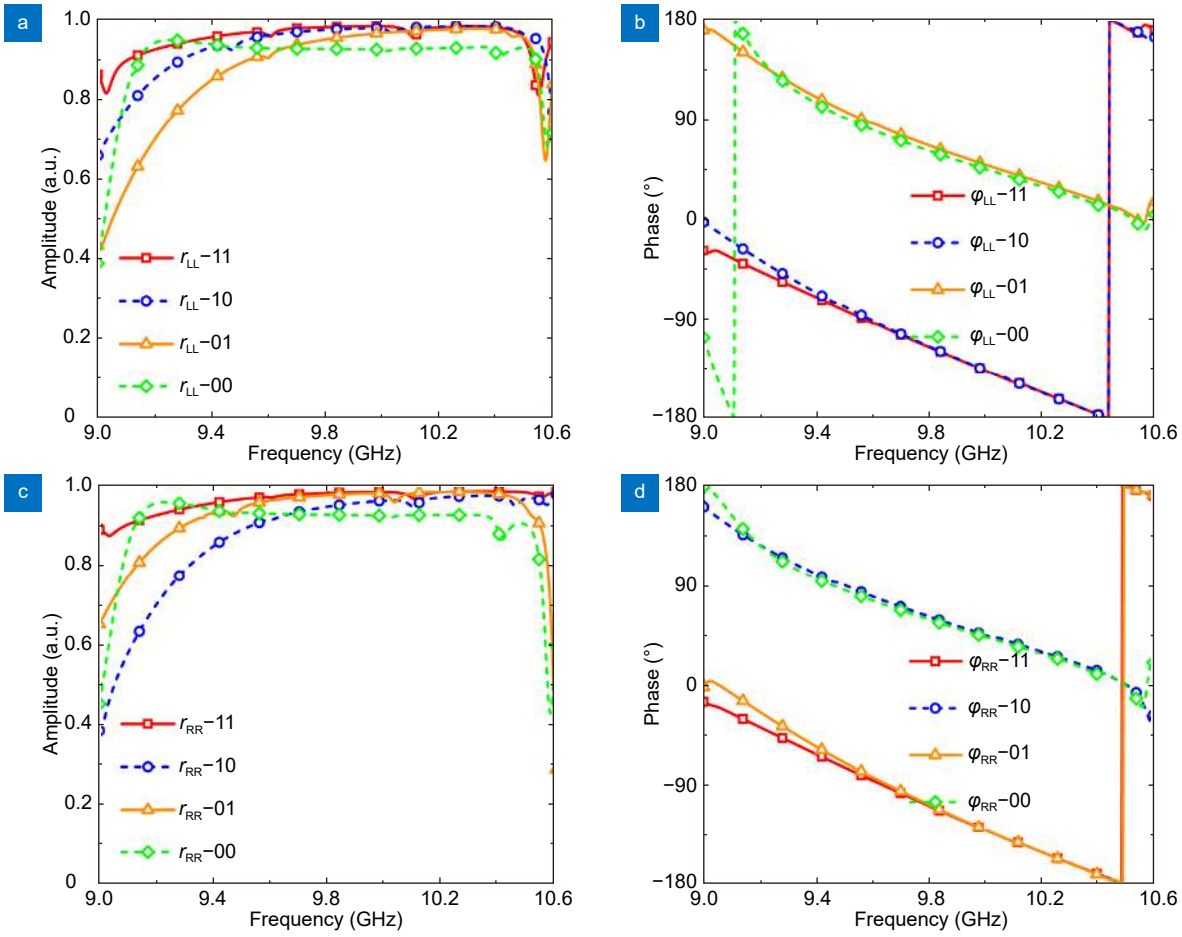

Fig. S6 | Reflection amplitude and phase responses of the 2×2 coding super-cell. (**a**, **b**) Simulated co-polarized reflection amplitude and phase responses of the proposed super-cell with coding states of "11", "10", "01", and "00" under LCP normal incidence, respectively. (**c**, **d**) Simulated co-polarized reflection amplitude and phase responses of the proposed super-cell with coding states of "11", "10", "01", and "00" under RCP normal incidence, respectively.

Section 7: Flow chart of the iterative optimization algorithm

The schematic of the iterative optimization algorithm is demonstrated in Fig. S7. The iterative optimization algorithm is a phase retrieval method, which establishes the correspondence between the phase distributions with known amplitude in the metasurface plane and the preset target image. In consideration of the phase distribution discontinuity of the coding meta-particle, the whole extraction process is mainly divided into phase iteration and phase discretization. The input contains the preset target image and initial amplitude and phase distributions in the metasurface plane, which is

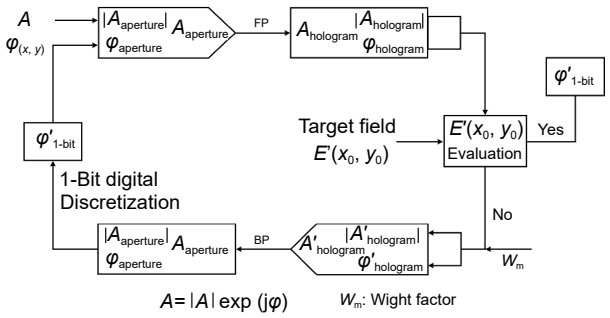

Fig. S7 | Demonstration of the flow chart of the iterative optimization algorithm.

separately precalculated (usually fixed at 1) and random (usually in the range of 0–2π). At first, the electric field intensity distributions of the metasurface aperture A_{aperture} is converted into electric field intensity distributions of the target holographic plane A_{hologram} via forward propagation (FP) formula. Herein, the propagation formula is proportional to Green function (e^{-jkr}/r) instead of Fraunhofer diffraction in the visible frequency. Subsequently, the calculated electric field intensity distribution A_{hologram} or $E'(x_0, y_0)$ is compared with the target electric field intensity $E(x_0, y_0)$ to determine whether phase meets the output requirements. To reduce the deviations between $E'(x_0, y_0)$ and $E(x_0, y_0)$ and improve the iteration convergence, a weight factor w_m is introduced to modulate the intensity ratio at the mth pixel and optimize the phase distribution on the metasurface. Then, the electric field intensity distributions of the target holographic plane A'_{hologram} is converted into electric field intensity distributions of the metasurface aperture A'_{aperture} via backward propagation (BP) formula, and the calculated $\varphi'_{\text{aperture}}$ is discretized to 1-bit (0 or π). The discretized phase distribution $\varphi_{\text{1-bit}}$ is input as the initial phase to the next iteration. The ordered and continuous iterations iteration will terminate and the final discretized phase distribution $\varphi'_{\text{1-bit}}$ can be obtained and exported until the calculated electric field intensity $E'(x_0, y_0)$ is very close to the target and cannot be improved anymore.

Section 8: Simulated and measured broadband performance of meta-holograms with identical focal length

The meta-holograms with identical focal length are simulated and measured under corresponding polarization channels in 9–10.5 GHz with a sample interval of 0.25 GHz, and the simulated and measured results presented in Fig. S8 indicate that the designed holograms can reconstruct the images of different letters in corresponding polarization channels despite the increased background noise due to the compensation phase departure of the meta-particles and measurement errors.

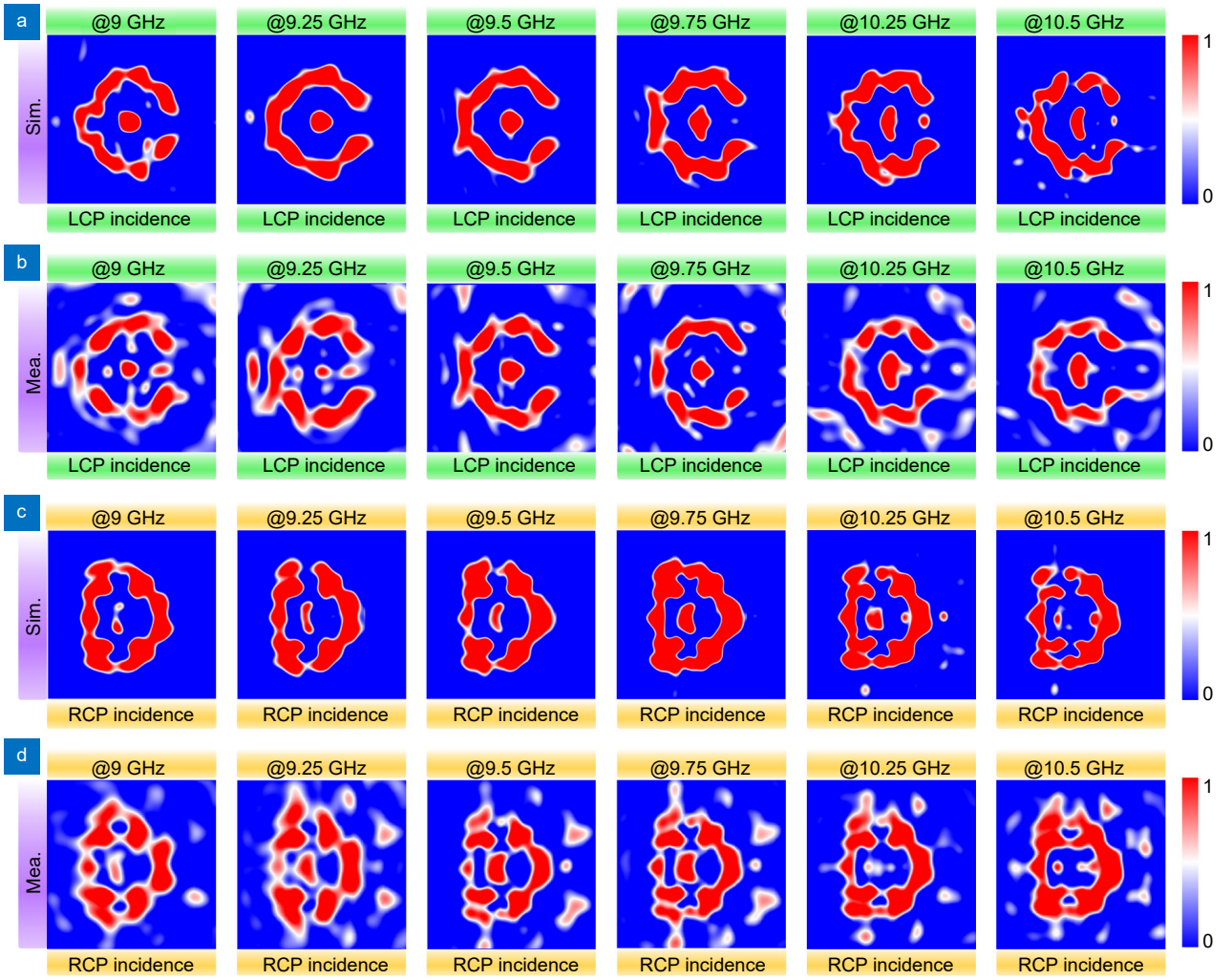

Fig. S8 | Broadband performance characterization of the meta-holograms with identical focal length. (**a**, **b**) Numerically simulated and experimentally measured normalized electric field intensity of LCP component utilizing corresponding coding pattern in L_r-L_i channel on the *x*-*y* plane cutting at *z*=100 mm in the frequency ranging from 9 to 10.5 GHz, respectively. (**c**, **d**) Numerically simulated and experimentally measured normalized electric field intensity of RCP component utilizing corresponding coding pattern in R_r-R_i channel on the *x*-*y* plane cutting at *z*=100 mm in the frequency ranging from 9 to 10.5 GHz, respectively.

The imaging efficiency and SNR of the meta-holograms with identical focal length for images of letters "C" and "D" are also investigated and separately illustrated in Fig. S9. The results further show the meta-holograms still maintain good imaging performances with relatively not low imaging efficiency and SNR, of which the imaging efficiency and SNR of both letters reach their peak at the designed working frequency of 10 GHz. But when the frequency is gradually shifted away from the designed working frequency, the imaging efficiency and SNR will deteriorate in various degrees, which is closely related to the characteristics of the meta-particle, and the imaging efficiency and SNR can be greatly improved via optimizing the geometric dimensions of the meta-particle to make it better meet amplitude conditions in a broader bandwidth.

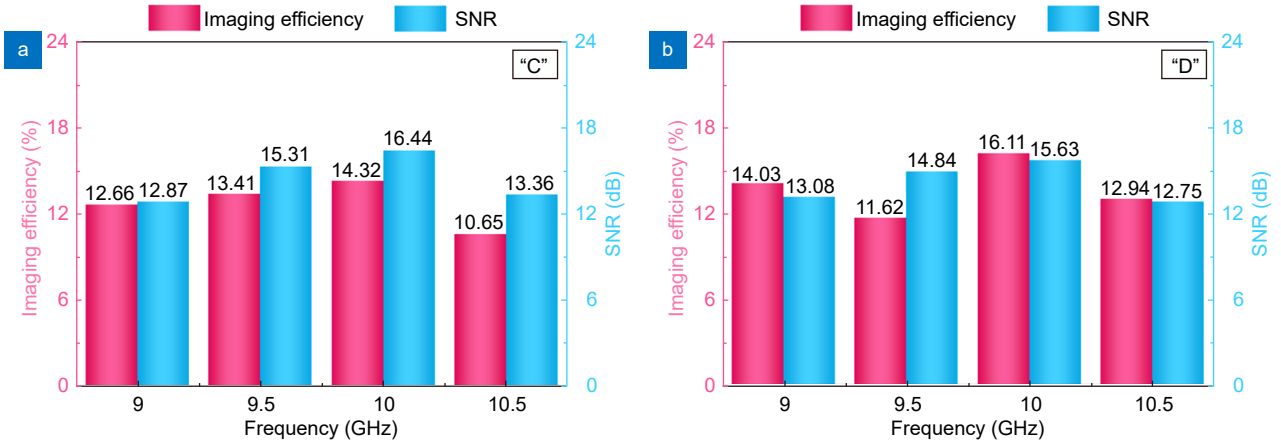

Fig. S9 | Measured imaging efficiency and SNR of the meta-holograms with identical focal length in the frequency range of 9–10.5 GHz for letters (a) "C" and (b) "D".

Section 9: Simulated and measured broadband performance of meta-holograms with variable focal length

The meta-holograms with variable focal length are simulated and measured under corresponding polarization channels in 9–10.5 GHz with a sample interval of 0.25 GHz, and the simulated and measured results presented in Fig. S10 indicate that the designed holograms can reconstruct the images of different letters in corresponding polarization channels despite the increased background noise due to the compensation phase departure of the meta-particles and measurement errors.

The imaging efficiency and SNR of the meta-holograms with variable focal length for images of letters "L" and "R" are also investigated and separately illustrated in Fig. S11. The results further show the meta-holograms still maintain good imaging performances with relatively not low imaging efficiency and SNR, of which the imaging efficiency and SNR of both letters reach their peak at the designed working frequency of 10 GHz. But when the frequency is gradually shifted away from the designed working frequency, the imaging efficiency and SNR will deteriorate in various degrees, which is closely related to the characteristics of the meta-particle, and the imaging efficiency and SNR can be greatly improved via optimizing the geometric dimensions of the meta-particle to make it better meet amplitude conditions in a broader bandwidth.

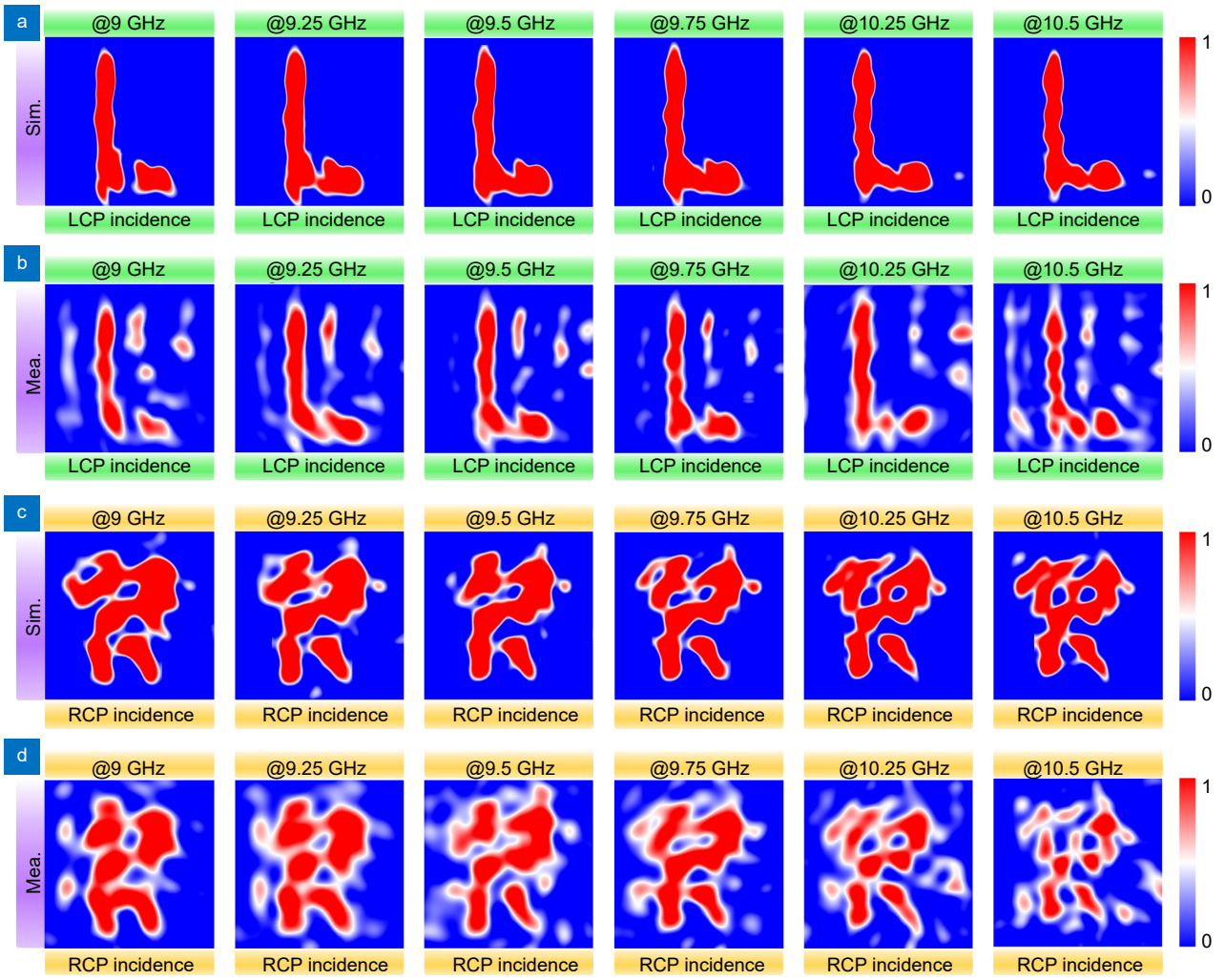

Fig. S10 | Broadband performance characterization of the meta-holograms with variable focal length. (**a**, **b**) Numerically simulated and experimentally measured normalized electric field intensity of LCP component utilizing corresponding coding pattern in L_r-L_i channel on the *x*-*y* plane cutting at *z*=100 mm in the frequency ranging from 9 to 10.5 GHz, respectively. (**c**, **d**) Numerically simulated and experimentally measured normalized electric field intensity of RCP component utilizing corresponding coding pattern in R_r-R_i channel on the *x*-*y* plane cutting at *z*=150 mm in the frequency ranging from 9 to 10.5 GHz, respectively.

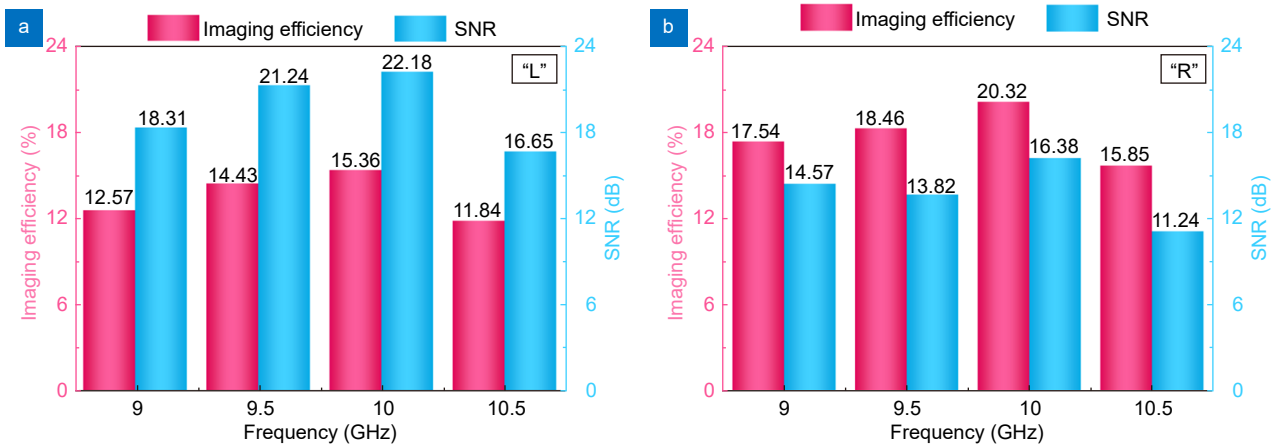

Fig. S11 | Measured imaging efficiency and SNR of the meta-holograms with variable focal length in the frequency range of 9–10.5 GHz for letters (a) "L" and (b) "R".

Section 10: Simulated and measured broadband performance of meta-holograms with switchable spatial pixels

The meta-holograms with switchable spatial pixels for LCP incidence and RCP incidence are simulated and measured under corresponding polarization channels in 9–10.5 GHz with a sample interval of 0.5 GHz, and the simulated and measured results presented in Fig. S12 and Fig. S13 indicate that the designed holograms can realize the scanning trajectory of predesigned image despite the increased background noise due to the compensation phase departure of the meta-particles and measurement errors.

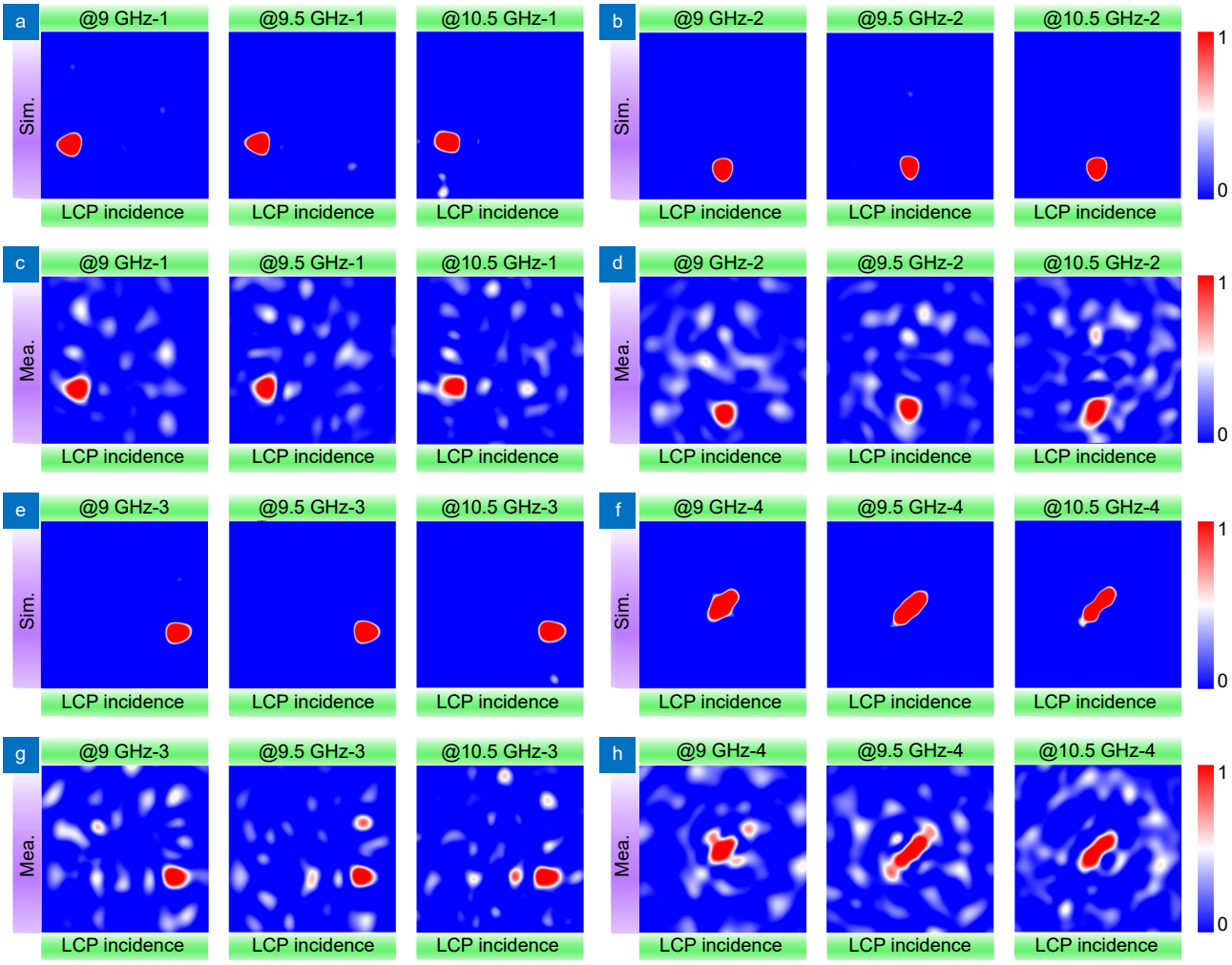

Fig. S12 | Broadband performance characterization of the meta-holograms with different spatial pixels in L_r-L_i channel. (**a**–**h**) Numerically simulated and experimentally measured normalized electric field intensity of LCP component utilizing coding pattern in corresponding channel for spatial pixels $\sigma_{-,1}$, $\sigma_{-,2}$, $\sigma_{-,3}$, and $\sigma_{-,4}$ on the *x*-*y* plane cutting at *z*=100 mm in the frequency ranging from 9 to 10.5 GHz, respectively.

The imaging efficiency and SNR of the meta-holograms with switchable spatial pixels for coplanar image of letter "S" are also investigated and separately illustrated in Fig. S14. The results further show the meta-holograms still maintain good imaging performances with relatively not low imaging efficiency and SNR, of which the imaging efficiency and SNR of both letters reach their peak at the designed working frequency of 10 GHz. But when the frequency is gradually shifted away from the designed working frequency, the imaging efficiency and SNR will deteriorate in various degrees, which is closely related to the characteristics of the meta-particle, and the imaging efficiency and SNR can be greatly improved via optimizing the geometric dimensions of the meta-particle to make it better meet amplitude conditions in a broader bandwidth.

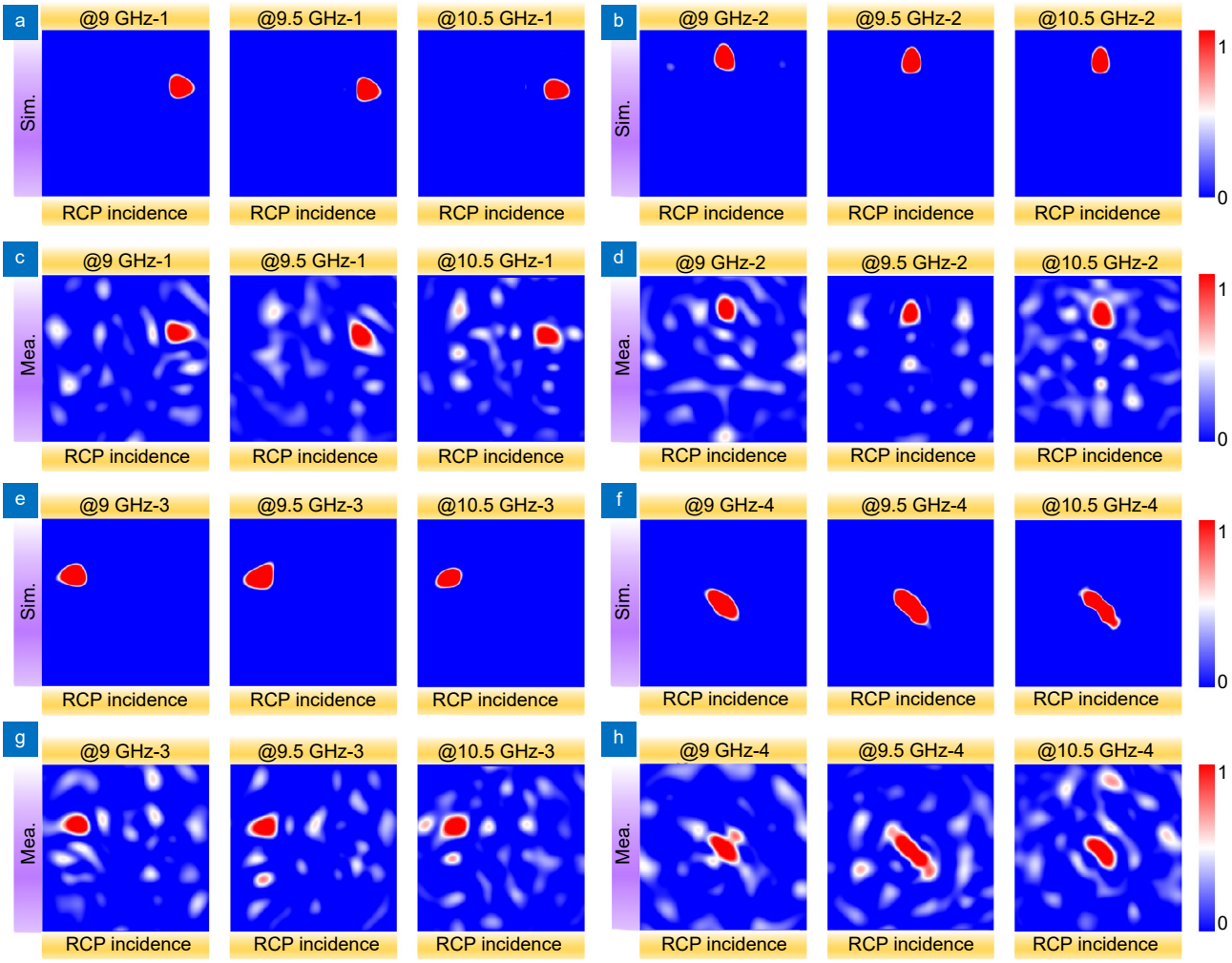

Fig. S13 | Broadband performance characterization of the meta-holograms with different spatial pixels in R_r-R_i channel. (**a**–**h**) Numerically simulated and experimentally measured normalized electric field intensity of RCP component utilizing coding pattern in corresponding channel for spatial pixels $\sigma_{+,1}$, $\sigma_{+,2}$, $\sigma_{+,3}$, and $\sigma_{+,4}$ on the *x*-*y* plane cutting at *z*=100 mm in the frequency ranging from 9 to 10.5 GHz, respectively.

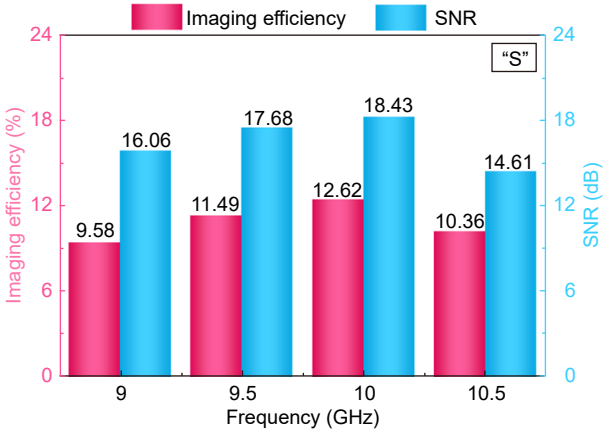

Fig. S14 | Measured imaging efficiency and SNR of the meta-holograms with switchable spatial pixels in the frequency range of 9-10.5 GHz for coplanar image of letter "S".

Section 11: Theoretical prediction of three groups of different meta-holograms and analysis and discussion

Three groups of different holograms are theoretically calculated under corresponding polarization channels at the fre-

quency of 10 GHz, and the predicted results presented in Fig. S15 indicate that the designed holograms can reconstruct the images of different letters utilizing predesigned phase coding patterns in corresponding polarization channels. Further synthesizing the simulated and measured results depicted in Fig. 3 and Fig. 4 of the main text, it's concluded that there are large differences in the measurement, mainly including relatively low imaging efficiency, background noise, and indistinct profile. The differences of the measured results may be caused by imperfect fabrication consisting of offset feeder line break and through hole size deviation, assembly errors of the metasurface consisting of partial virtual welding of active components with certain volume and the measurement errors consisting of coaxial probe occlusion, misalignment of dual LP measurement, and some man-made accidental factors during the experiment. To solve these problems, in the follow-up work, we plan to adopt some methods such as the miniaturized periodic structure, the large metasurface array aperture and multi-bit phase distributions with uniform magnitudes provided by varactor and varistor diodes, and multiple measurements for reducing the unintentional factors.

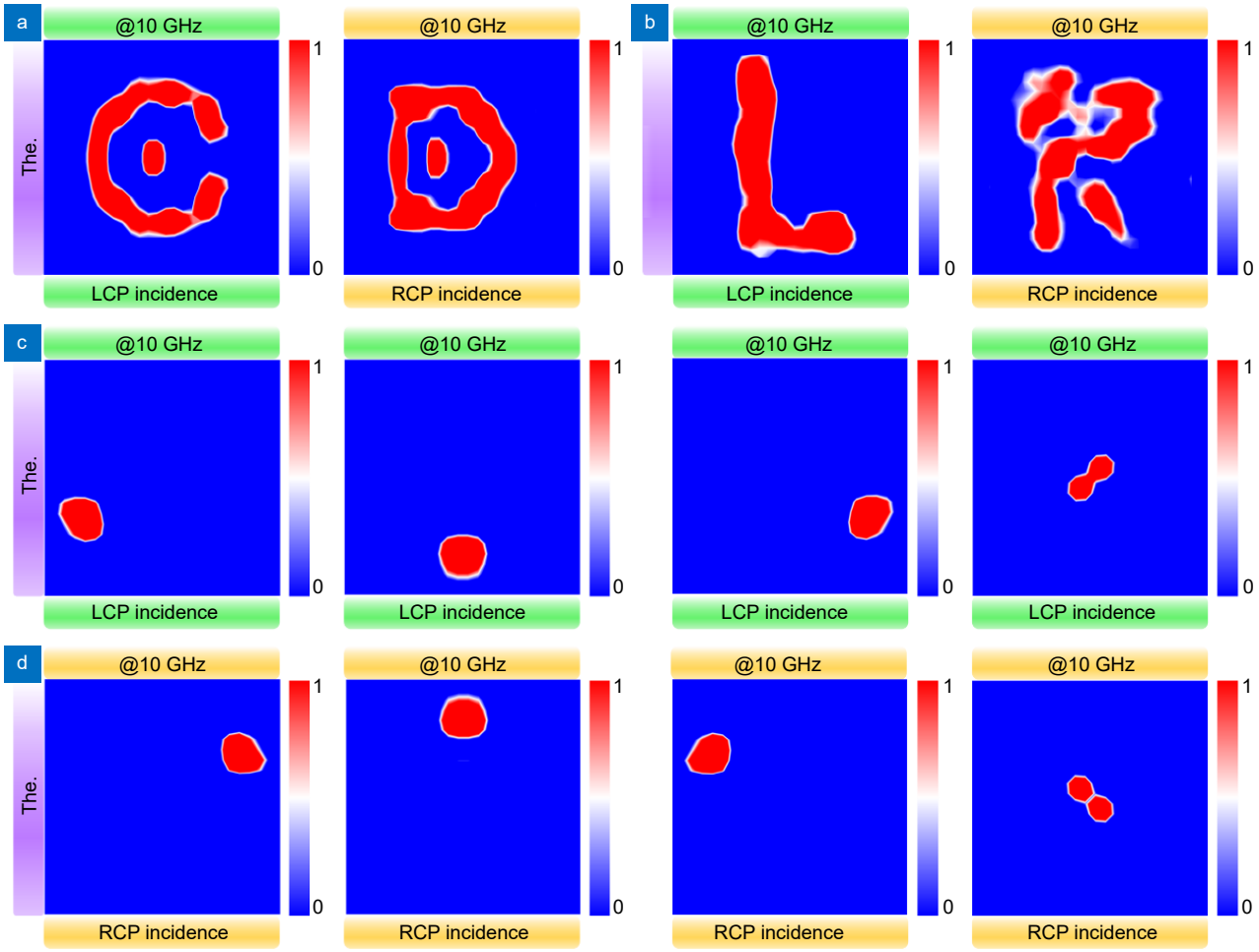

Fig. S15 | Theoretical prediction for the generation of different types of meta-holograms. (**a**) The theoretically calculated normalized electric field intensity of LCP component for target images "C" (left panel) in L_r-L_i channel and of RCP component "D" (right panel) in R_r-R_i channel cutting at z=100 mm on the x-y plane. (**b**) The theoretically calculated normalized electric field intensity of LCP component for target images "L" (left panel) in L_r-L_i channel cutting at z=100 mm and of RCP component "R" (right panel) in R_r-R_i channel cutting at z=150 mm on the x-y plane, respectively. (**c**–**d**) The theoretically calculated normalized electric field intensity of LCP component for spatial pixel $\sigma_{-,1}$, $\sigma_{-,2}$, $\sigma_{-,3}$, and $\sigma_{-,4}$ (upper row) and of RCP component for $\sigma_{+,1}$, $\sigma_{+,2}$, $\sigma_{+,3}$, and $\sigma_{+,4}$ (bottom row) cutting at z=100 mm on the x-y plane.

Section 12: Holographic imaging manipulation principle under orthogonal LP conversion channels

According to Eqs. (S10) and (S11), when the meta-particles are in the states "10" or "01", i.e., the PIN diodes in the left and right arms are respectively in the "ON/OFF" or "OFF/ON" states, the 1-bit cross-polarized phase modulation can be

achieved under orthogonal LP incidence. To validate the feasibility of the above theoretical analysis, two different target holographic images: numbers "1" and "3" are prestored in X_r-Y_i channel and Y_r-X_i channel based on the above CBR-CM, as shown in Fig. S16(a). Through the calculation of the iterative optimization algorithm, we further obtain the corresponding phase coding patterns with reference frequency of f=10 GHz and imaging plane of z=100 mm, as depicted in Fig. S16(b). Correspondingly, for the phase coding patterns in LCP and RCP channels, as long as the phase of each point in one polarization channel is consistent with the LP conversion channels, i.e., the pre-designed phase patterns, and the phase of that in another polarization channel keeps the difference value of π. The simulated results are exhibited in Fig. S16(c–e), from which the predesigned holographic images are distinctly seen being reconstructed spatially in the near field and in good accordance with the theoretical prediction.

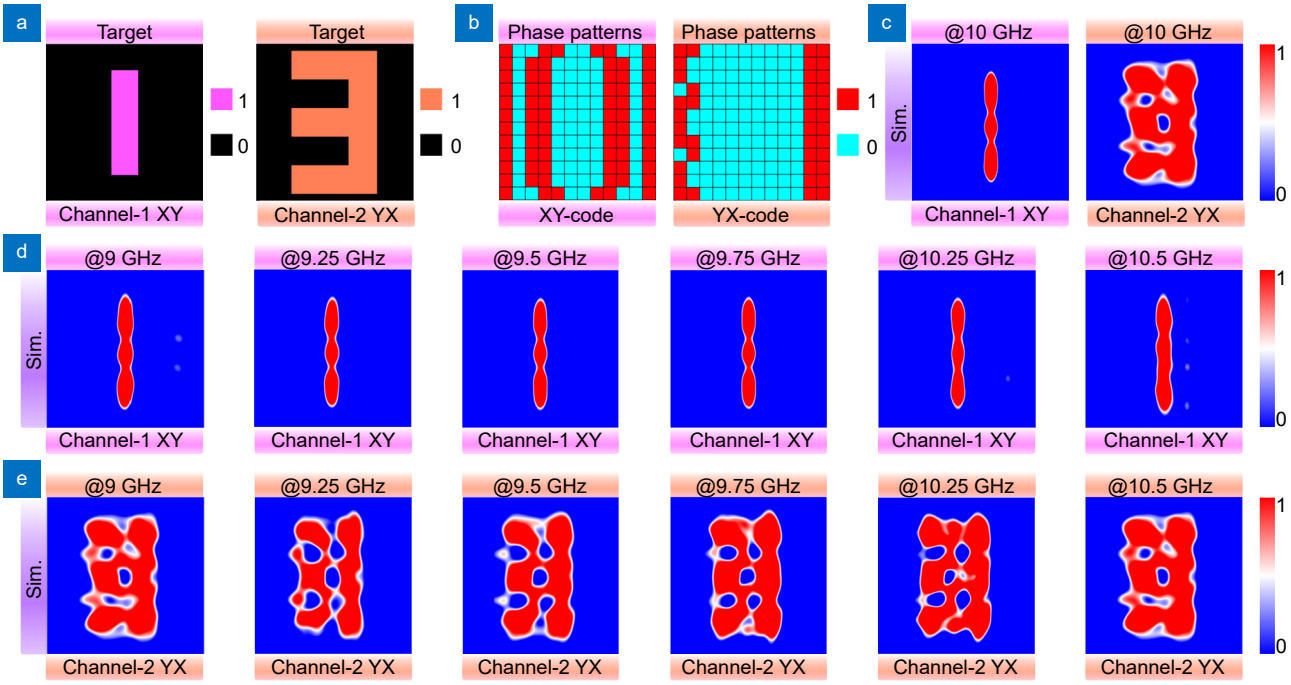

Fig. S16 | Directional generation of meta-holograms under orthogonal LP conversion channels. (**a**) The target monochrome image of the number "1" in X_r-Y_i channel and the number "3" in Y_r-X_i channel. (**b**) The calculated phase coding patterns in corresponding LP conversion channels. (**c**) Numerically simulated normalized electric field intensity of *x*-LP component utilizing coding pattern in b in X_r-Y_i channel and normalized electric field intensity of *y*-LP component utilizing coding pattern in b in Y_r-X_i channel at 10 GHz on the *x*-*y* plane cutting at *z*=100 mm. (**d**, **e**) Simulated holographic images of the number "1" and the number "3" in corresponding LP conversion channels at corresponding imaging planes with frequency ranging from 9 to 10.5 GHz.

Section 13: Simulated and measured broadband performance of meta-holograms against arbitrary polarization states on Poincaré sphere

The meta-holograms against arbitrary polarization states on Poincaré sphere are simulated and measured under corresponding polarization channels in 9–10.5 GHz with a sample interval of 0.5 GHz, and the simulated and measured results presented in Fig. S17 and Fig. S18 indicate that the designed holograms can realize the scanning trajectory of predesigned image despite the increased background noise due to the compensation phase departure of the meta-particles and measurement errors.

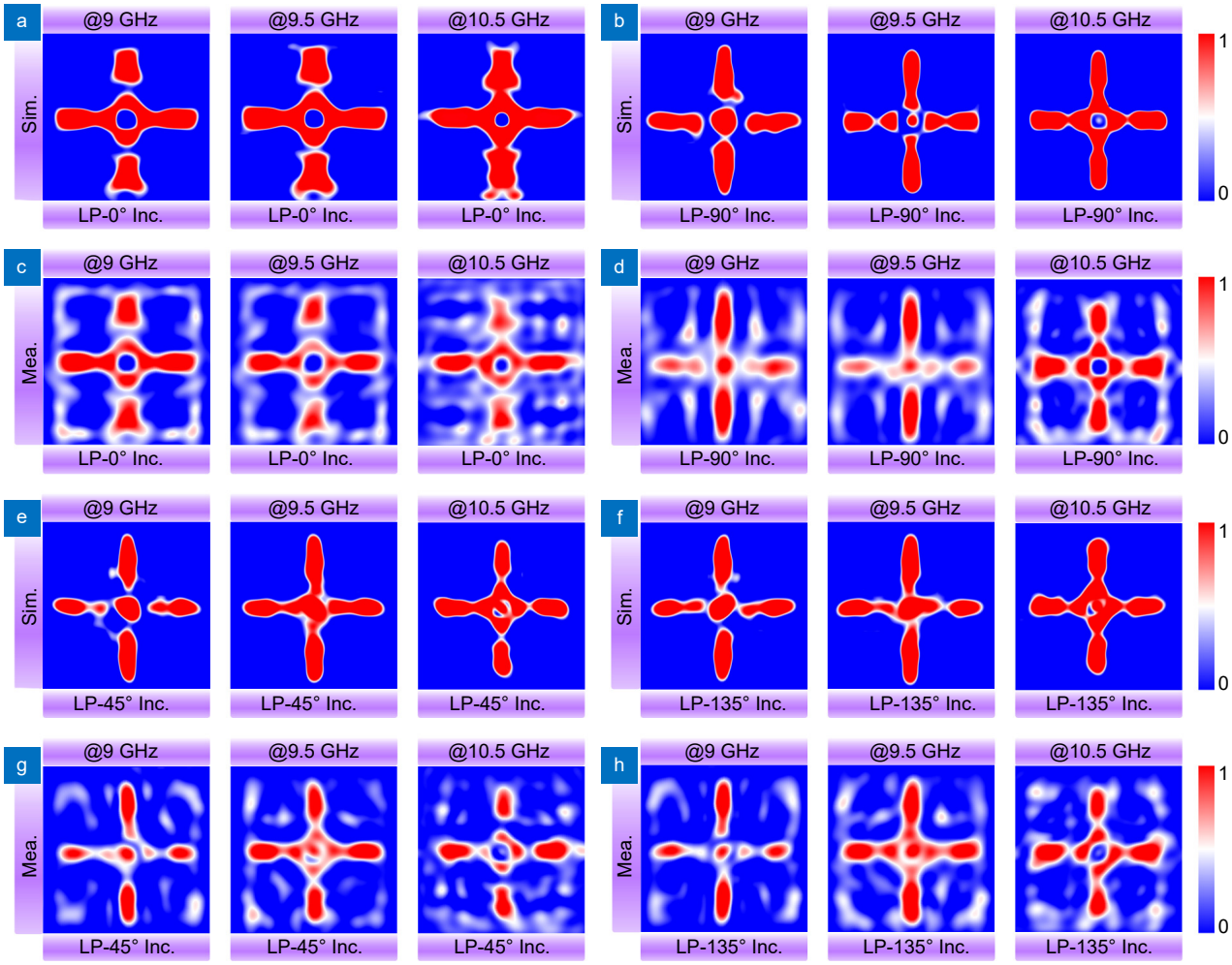

Fig. S17 | Broadband performance characterization of the meta-holograms against four typical LP states on Poincaré sphere. (**a**–**d**) Numerically simulated and experimentally measured normalized electric field intensity encoded with LP-0° and LP-90° states on the *x*-*y* plane cutting at *z*=100 mm in the frequency ranging from 9 to 10.5 GHz, respectively. (**e**–**h**) Numerically simulated and experimentally measured normalized electric field intensity encoded with LP-45° and LP-135° states on the *x*-*y* plane cutting at *z*=100 mm in the frequency ranging from 9 to 10.5 GHz, respectively.

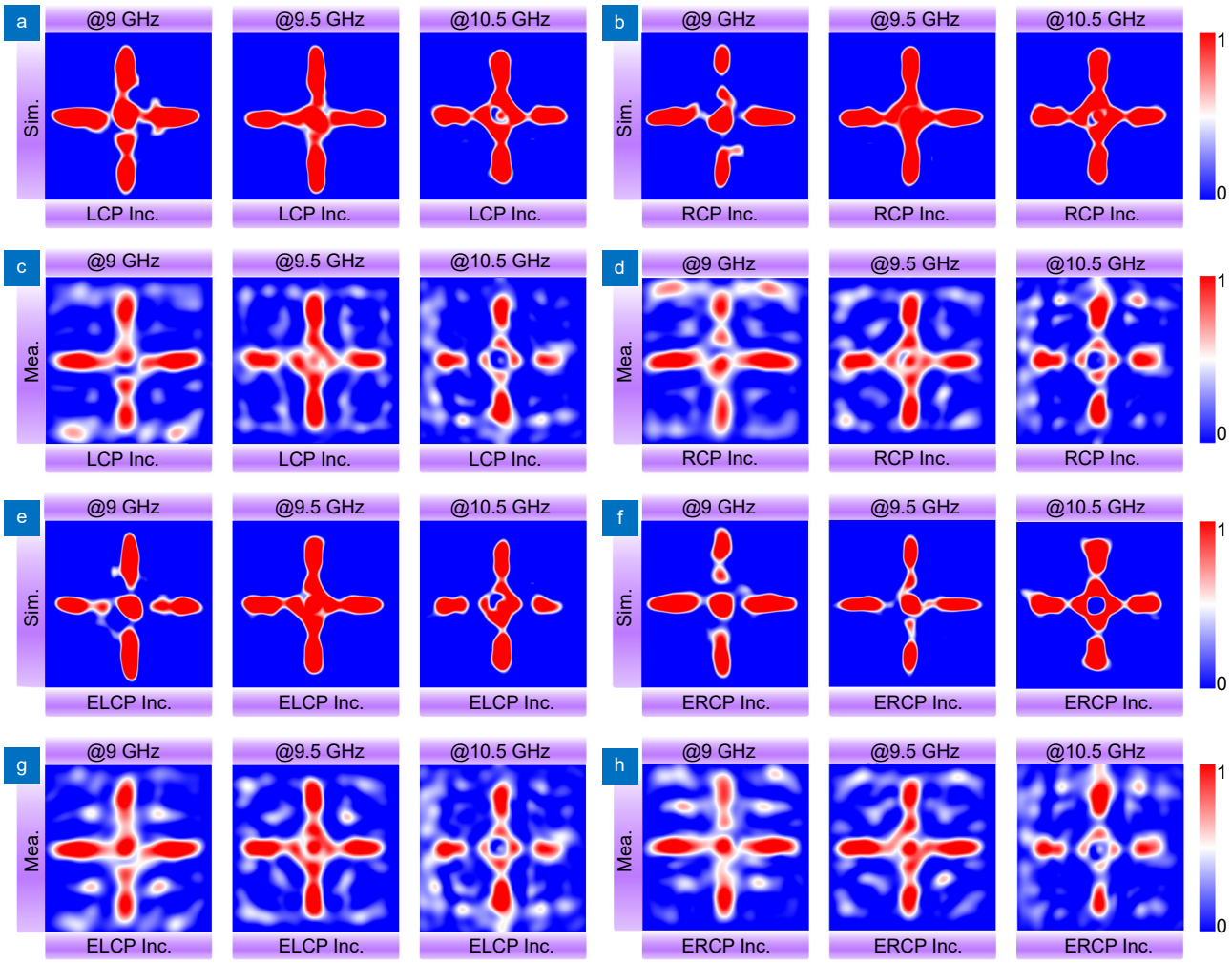

Fig. S18 | Broadband performance characterization of the meta-holograms against two typical CP and EP states on Poincaré sphere. (**a**–**d**) Numerically simulated and experimentally measured normalized electric field intensity encoded with LCP and RCP states on the *x*-*y* plane cutting at *z*=100 mm in the frequency ranging from 9 to 10.5 GHz, respectively. (**e**, **f**) Numerically simulated and experimentally measured normalized electric field intensity encoded with ELCP and ERCP states on the *x*-*y* plane cutting at *z*=100 mm in the frequency ranging from 9 to 10.5 GHz, respectively.

Section 14: Performance comparison of the proposed CBR-CM with previous works of reprogrammable metasurfaces

The studies in ref.[S1–S5] are mostly limited to single polarization, and loss of single element and the total size of the metasurface prototypes are relatively large, which is not conducive to the development of modern efficient and integrated devices. In addition, the reprogrammable metasurfaces proposed in the ref.[S6–S10] operate in multi-polarization reconfigurable modes. However, more active components embedded into one element will result in a more complex external hardware network, meanwhile, it's worth noting that the operating bandwidth and addressing mode cannot be taken into account in the same model simultaneously. The advantages and improvements of our work propose novel complete-basis-reprogrammable coding metasurface under incident full polarized waves in CP basis form. What's more, compared with other relevant works, the number of the active components embedded in one element has been cut in half, reducing the loss and complexity of the bias circuit. Therefore, each element (elementary unit) is able to be efficiently and independently addressed and possesses considerably operating bandwidth.

Table S1 | Performance comparison of the proposed CBR-CM with previous works of reprogrammable metasurfaces.

Ref. and year	Mode of operation	Polarization	Number of elements	Number of diodes in one element	Total size (mm^3)	Individually Addressed	Element Loss (dB)	Operation efficiency	Frequency band (GHz)
ref.[1], 2023	Reflection	LP	16×16	4	296.8×283.4×2.115	Yes	2.25	N.A.	7.5–9.5
ref.[2], 2024	Reflection	LP	16×30	1	420×240×1.52	Yes	<1.5	N.A.	4.611
ref.[3], 2021	Reflection	LP	30×30	1	180×180×1.25	Yes	2.5	24.8%–42.5%	8.5–9.5
ref.[4], 2024	Reflection & Transmission	LP	12×12	3	420×420×4.2	Yes	<0.5	N.A.	3.35–3.65
ref.[5], 2021	Reflection	CP	32×32	4	200×200×N.A.	Yes	<1	N.A.	6.84–7.13
ref.[6], 2022	Reflection	Dual LP	20×20	4	320×320×4.43	Yes	<0.3	15.47%	7.45
ref.[7], 2020	Reflection	Dual LP, Dual CP	24×24	4	260×260×3.37	No	<1	N.A.	5.67–6.15
ref.[8], 2024	Reflection	Dual LP, Dual CP	16×16	4	300×300×4.5	No	1.7	N.A.	7.0–11.1
ref.[9], 2023	Reflection	Dual LP, Dual CP	16×16	2	220×220×3.58	Yes	<1.1	20.1%–24.5%	13.5
Ref.[10], 2022	Transmission	Dual LP, Dual CP	12×12	8	202×202×5	Yes	<1	N.A.	7.4
This work	Reflection	Full Polarization	24×24	2	260×250×4.43	Yes	<1	12.6%–20.3%	9.0–10.5

Section 15: Diagram of the FPGA-based control circuit

The schematic diagram of the FPGA-based control circuit is depicted in Fig. S19.

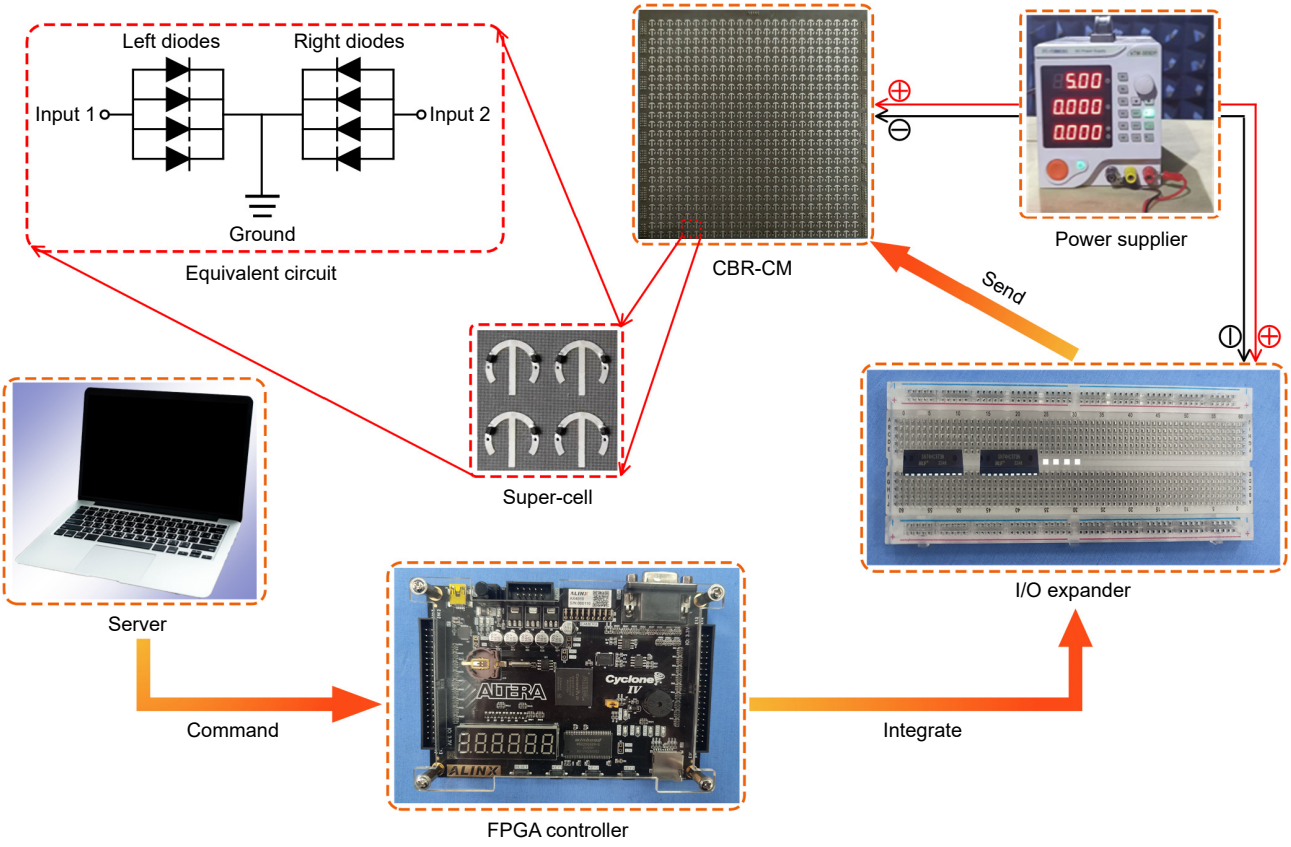

Fig. S19 | Diagram of the FPGA-based control circuit.

Section 16: The photographs of fabricated metasurface and experimental setup

The pictures of the fabricated prototype are displayed in Fig. 20(a) and 20(b), where the zoom-in view displays the 4×4 local coding meta-particles with soldered PIN diodes. Figure 20(c–f) illustrate the near-field experimental setups under CP or LP incidence.

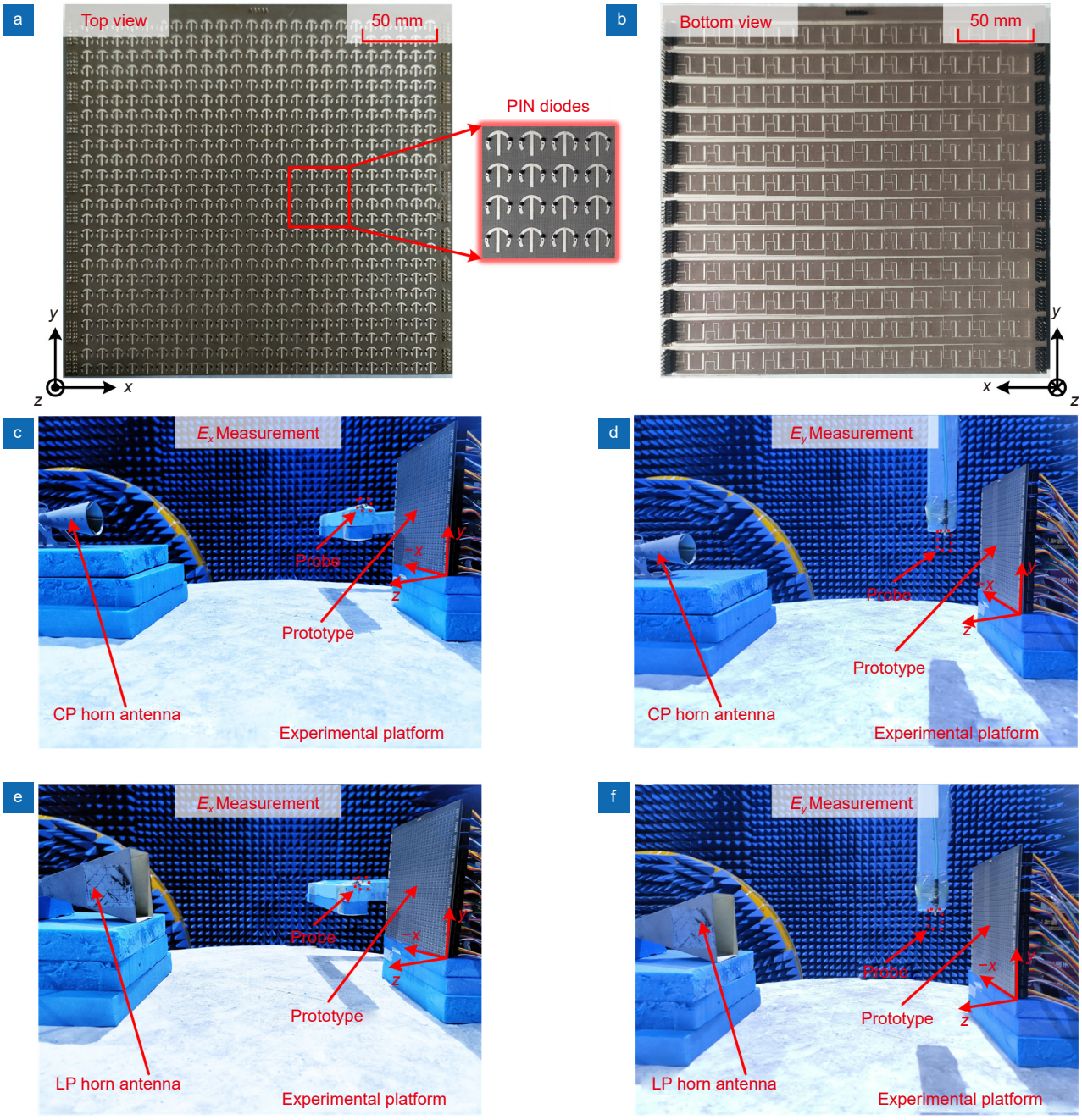

Fig. S20 | Prototype fabrication, and experimental characterization of the CBR-CM prototype. (**a**, **b**) Top view and bottom view of the fabricated prototype, where the inset exhibits 4×4 local coding meta-particles with soldered PIN diodes. (**c**, **d**) The near-field experimental setups for measuring E_x and E_y components in microwave anechoic chamber under CP normal incidence. (**e**, **f**) The near-field experimental setups for measuring E_x and E_y components in microwave anechoic chamber under LP normal incidence.

References

S1. Tian HW, Xu L, Li X et al. Integrated control of radiations and in - band Co - polarized reflections by a single programmable metasurface. *Adv Funct Mater* **33**, 2302753 (2023).

S2. Zeng BW, Li CX, Fang B et al. Flexible tuning of multifocal holographic imaging based on electronically controlled metasurfaces. *Photonics Res* **12**, 61–69 (2024).
S3. Feng R, Ratni B, Yi JJ et al. Versatile metasurface platform for electromagnetic wave tailoring. *Photonics Res* **9**, 1650–1659 (2021).
S4. Yin T, Ren J, Zhang B et al. Reconfigurable transmission‐reflection‐integrated coding metasurface for full‐space electromagnetic wavefront manipulation. *Adv Opt Mater* **12**, 2301326 (2024).
S5. Jiang LX, Jing Y, Li YF et al. Multidimensionally manipulated active coding metasurface by merging pancharatnam–berry phase and dynamic phase. *Adv Opt Mater* **9**, 2100484 (2021).
S6. Zhang N, Chen K, Zhao JM et al. A dual-polarized reconfigurable reflectarray antenna based on dual-channel programmable metasurface. *IEEE Trans Antennas Propag* **70**, 7403–7412 (2022).
S7. Zhang XG, Yu Q, Jiang WX et al. Polarization‐controlled dual‐programmable metasurfaces. *Adv Sci* **7**, 1903382 (2020).
S8. Liu W, Dai JY, Zhang YM et al. Wideband polarization‐insensitive 1‐Bit phase manipulations with Co‐and cross‐polarized conversions for LP and CP waves. *Laser Photonics Rev* 2400049 (2024); http://doi.org/10.1002/lpor.202400049.
S9. Yu H, Zhang ZY, Su JX et al. Quad-polarization reconfigurable reflectarray with independent beam- scanning and polarization switching capabilities. *IEEE Trans Antennas Propag* **71**, 7285–7298 (2023).
S10. Wang CH, Xu HX, Wang YZ et al. Reconfigurable transmissive metasurface synergizing dynamic and geometric phase for versatile polarization and wavefront manipulations. *Mater Des* **225**, 111445 (2023).